Spin-orbit relaxation of cesium 7 ^2D in mixtures of helium and argon

Ricardo C. Davila* and Glen P. Perram†
Department of Engineering Physics, Air Force Institute of Technology, Wright-Patterson AFB, Ohio 45433-7765, USA
(Received 1 January 2016; published 23 March 2016)

Pulsed excitation on the two-photon Cs $6\,^2S_{1/2} \rightarrow 7\,^2D_{3/2,5/2}$ transition results in time-resolved fluorescence at 697 and 672 nm. The rates for fine-structure mixing between the $7\,^2D_{3/2,5/2}$ states have been measured for helium and argon rare-gas collision partners. The mixing rates are very fast, $1.26 \pm 0.05 \times 10^{-9}$ cm^3/atom s for He and $1.52 \pm 0.05 \times 10^{-10}$ cm^3/atom s for Ar, driven by the small energy splitting and large radial distribution for the valence electron. The quenching rates are considerably slower, $6.84 \pm 0.09 \times 10^{-11}$ and $2.65 \pm 0.04 \times 10^{-11}$ cm^3/atom s for He and Ar, respectively. The current results are placed in context with similar rates for other alkali-metal–rare-gas collision pairs using adiabaticity arguments.

DOI: 10.1103/PhysRevA.93.033418

I. INTRODUCTION

Despite an optically pumped potassium vapor laser being proposed by Schawlow and Townes in 1958 [1], it was not until 2003 that the first efficient, diode pumped lasing in rubidium (Rb) and cesium (Cs) vapors were achieved [2,3]. The diode pumped alkali laser (DPAL), a three-level laser system, is pumped by diode bars or stacks through the alkali metal's D_2 transition to its $^2P_{3/2}$ state, then collisionally relaxed to the $^2P_{1/2}$ state where it lases in the near-infrared (NIR) along the D_1 transition. Lasing is achieved at 770 nm (K), 795 nm (Rb), and 894 nm (Cs). DPAL performance is optimized when spin-orbit relaxation, with the help of a buffer gas (usually a rare gas or small hydrocarbon), is much faster than the optical excitation rate [4–6]. Several comprehensive DPAL reviews [4,7,8] outline the benefits of this laser's high quantum efficiency, gaseous gain medium, reduced thermal issues, diode pumping, and scalability to high output powers.

Several optically pumped alkali lasers operating at alternative wavelengths have also been demonstrated and require excitation above the first $^2P_{3/2}$ excited state [9–18]. Optically pumped alkali lasers at far- mid-, and near-infrared, visible, and ultraviolet wavelengths may be useful as beacons or illuminators for laser weapons, or for infrared countermeasures [19]. Like the traditional DPAL, these higher energy states require knowing the transition rates, optical cross sections, collisional quenching, and spin-orbit rates to understand the competing and cascading laser transitions. One such excitation scheme, depicted in Fig. 1, involves two-photon direct excitation of the Cs ground state to Cs $7\,^2D_{5/2,3/2}$ followed by primary infrared and visible transitions to the Cs $8\,^2P$, Cs $7\,^2P$, and Cs $6\,^2P$ and secondary ultraviolet, blue, and NIR transitions to the Cs $6\,^2S_{1/2}$ ground state. Indeed, blue lasers have been demonstrated by optically pumping in the near infrared using this scheme [16,18]. However, the fine-structure spin-orbit and collisional quenching rates of the Cs $7\,^2D_{5/2,3/2}$ states have not been reported. Excitation from the Cs $6\,^2D_{1/2} \rightarrow 7\,^2D_{5/2,3/2}$ states by two-photon transitions has been performed to determine hyperfine coupling constants for Cs $7\,^2D$ states [20,21].

A thorough investigation of the fine-structure mixing rate database for $8\,^2P$, $7\,^2P$, and $6\,^2P$ states in alkali-metal vapor collisions with rare gases reveals that fine-structure mixing rates increase with deceased energy splitting [22] and is consistent with previous adiabaticity studies [23]. Although Ref. [22] does not include high-lying excited alkali-metal states such as Cs $7\,^2D$, it is predicted that Cs $7\,^2D$ will exhibit more impulsive collisions with rare gases leading to faster spin-orbit rates. In this work, time-resolved laser-induced fluorescence techniques are used to measure fine-structure mixing rates for the Cs $7\,^2D_{5/2,3/2}$ states with He and Ar rare-gas collision partners.

II. KINETIC ANALYSIS

The transitions considered for exciting the $7\,^2D_{3/2,5/2}$ levels of the cesium atom by two-photon absorption with a buffer gas are illustrated in Fig. 2. The radiative decay rates from states $|2\rangle$,$|1\rangle$ to the ground state $|0\rangle$ are labeled as Γ_{20} and Γ_{10}. The collisional mixing rates from states $|2\rangle \rightarrow |1\rangle$ and $|1\rangle \rightarrow |2\rangle$ are labeled as R_{21} and R_{12}, respectively. The mixing rates R_{12} and R_{21} adhere to the principle of detailed balance:

$$\frac{R_{12}}{R_{21}} = \frac{g_2}{g_1} e^{-\Delta E/k_b T} = \rho, \tag{1}$$

where $g_2 = 6$ and $g_1 = 4$ represent the degeneracies of the respective $7\,^2D_{5/2,3/2}$ atomic states, ΔE is the energy difference between these states (21 cm^{-1} for the $7\,^2D$ states), k_b is the Boltzmann constant, and T is the temperature. For these same states and a temperature of 50 °C, $\rho = 1.65$.

The spin-orbit mixing rate is related to the thermally averaged collision cross section σ_{21} via the average relative speed of the collision pair $\overline{v}$:

$$R_{21} = (n)(\sigma_{21})(\overline{v}) = (n)k_{21}, \tag{2}$$

where n is the rare-gas density and k_{21} is the spin-orbit mixing rate coefficient. For Cs at 50 °C with collision partners He and Ar, the mean relative velocities are 1.3×10^5 cm/s for [Cs,He] and 4.7×10^4 cm/s for [Cs,Ar]. Last, the collisional quenching rates associated with the depopulation of states $|2\rangle$ and $|1\rangle$ to the ground state $|0\rangle$ are labeled Q_{20} and Q_{10}.

The time evolution of the population densities in states $|2\rangle$ and $|1\rangle$ after pulsed excitation is described by the first-order

*ricardo.davila@afit.edu
†glen.perram@afit.edu

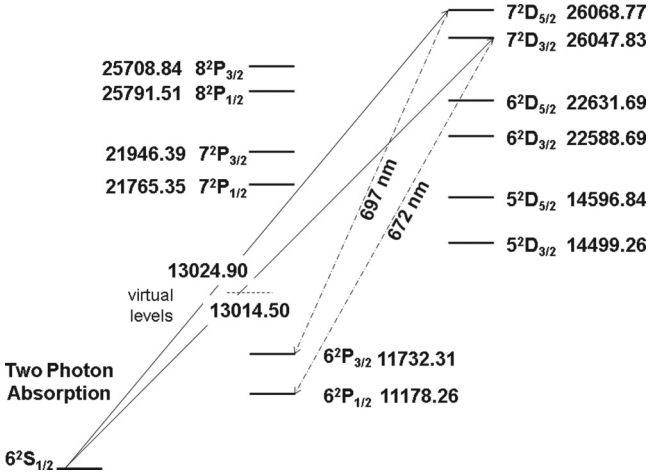

FIG. 1. Cs energy level diagram.

differential equations:

$$\frac{dn_2(t)}{dt} = -(\Gamma_{20} + R_{21} + Q_{20})n_2(t) + R_{12}n_1(t), \quad (3)$$

$$\frac{dn_1(t)}{dt} = -(\Gamma_{10} + R_{12} + Q_{10})n_1(t) + R_{21}n_2(t). \quad (4)$$

Defining $\alpha_2 = -(\Gamma_{20} + R_{21} + Q_{20})$ and $\alpha_1 = -(\Gamma_{10} + R_{12} + Q_{10})$, the general solution takes the form of a double exponential

$$n_1(t) = A\, e^{\lambda_+ t} + B\, e^{\lambda_- t}, \quad (5)$$

where λ_+ and λ_- are given by the eigenvalues [12,24,25]

$$\lambda_\pm = \tfrac{1}{2}\{-(\alpha_1 + \alpha_2) \pm \sqrt{(\alpha_1 - \alpha_2)^2 + 4R_{12}R_{21}}\}. \quad (6)$$

For initial conditions where the near-instantaneous pump populates the $7\ ^2D_{5/2}$ state, $n_1(t=0) = 0$ and $n_2(t=0) > 0$, the solutions for the parent n_2 and satellite n_1 states become

$$n_1(t) = A(\, e^{\lambda_+ t} - e^{\lambda_- t}), \quad (7)$$

$$n_2(t) = \frac{A\left[(\alpha_1 + \lambda_+)\, e^{\lambda_+ t} - (\alpha_1 + \lambda_-)\, e^{\lambda_- t}\right]}{R_{21}}. \quad (8)$$

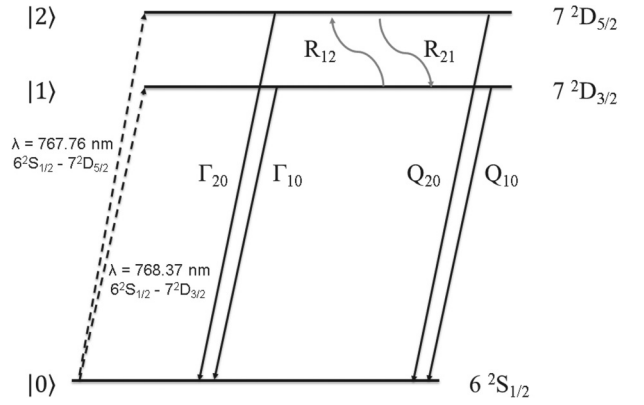

FIG. 2. Cesium energy levels for the $7\,^2D$ fine-structure collisional mixing.

For high rare-gas densities where $R_{12} - R_{21} \gg \Gamma_{10} - \Gamma_{20}$ and assuming $Q_{10} = Q_{20} = Q$, Eq. (6) can be approximated in this limit as [12,24,25]

$$\lambda_+ = \frac{\Gamma_{10} + \Gamma_{20}}{2} - \left(\frac{\rho - 1}{\rho + 1}\right)\frac{\Gamma_{10} - \Gamma_{20}}{2} + \sigma_Q(n)(\overline{v}), \quad (9)$$

$$\lambda_- = \frac{\Gamma_{10} + \Gamma_{20}}{2} + \left(\frac{\rho - 1}{\rho + 1}\right)\frac{\Gamma_{10} - \Gamma_{20}}{2} + [\sigma_Q + \sigma_{21}(\rho + 1)](n)(\overline{v}), \quad (10)$$

where ρ is given by Eq. (1) and σ_{21} by Eq. (2), $\sigma_Q = Q/[(n)(\overline{v})]$, and we define $k_Q = \sigma_Q(n)$ as the quenching rate coefficient.

The fine-structure transition probability can be defined by the ratio of the experimentally measured cross section σ_{21} and the quantum defect cross section σ_{QD},

$$P = \frac{\sigma_{21}}{\sigma_{\mathrm{QD}}} \quad (11)$$

with

$$\sigma_{\mathrm{QD}} = \pi(\langle r\rangle + r_{\mathrm{RG}})^2, \quad (12)$$

where $\langle r\rangle$ is the expectation value of the Cs atom's electron position and r_{RG} is the effective radius of the rare-gas atom [22]. Since the alkali metals are well represented by hydrogenic approximations [26], the expectation value of the electron position is given by

$$\langle r\rangle = a_\mu(n^*)^2\left[1 + \frac{1}{2}\left(1 - \frac{l(l+1)}{(n^*)^2}\right)\right], \quad (13)$$

where a_μ is the effective Bohr radius of the alkali metal, l is the angular momentum quantum number, and n^* is the effective quantum number given by

$$n^* = \sqrt{\frac{E_{\mathrm{Ryd}}}{T - E}}, \quad (14)$$

In Eq. (14) E_{Ryd} is the Rydberg energy (109737.32 cm^{-1}), T is the ionization energy, and E is the energy level corresponding to the effective quantum number. The effective quantum numbers for $7\ ^2D_{5/2,3/2}$ are 4.53 and 4.52, respectively.

The extent to which the alkali-metal doublet transfer collision with the rare-gas species is sudden or adiabatic depends on the interatomic velocity as well as the spin-orbit splitting [23]. For the alkali-metal–rare-gas collision the adiabaticity is defined as [27]

$$\zeta = \frac{\tau_c}{\tau_v} = \frac{\Delta L}{\overline{v}}, \quad (15)$$

where τ_c is the duration of the collision, τ_v is the period of oscillation, Δ is the spin-orbit splitting, L is the interaction length, and $\overline{v}$ is the mean relative speed. We choose to set the interaction length L at 10 Å. When the duration of the collision is short, the time-dependent perturbation is not averaged out due to oscillations in the state dynamics and a higher probability for energy transfer is achieved.

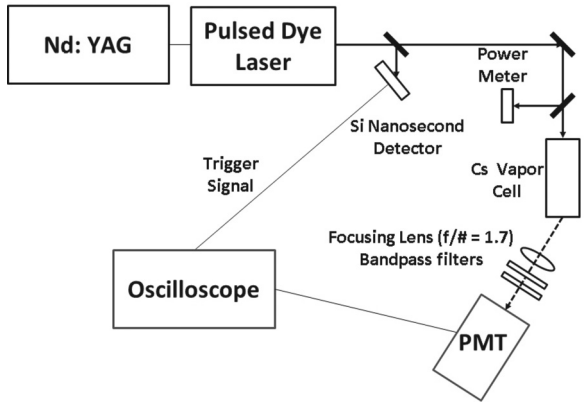

FIG. 3. Temporally resolved laser-induced fluorescence apparatus.

III. EXPERIMENT

The apparatus for the two-photon kinetic study for the $7\,^2D_{5/2,3/2} \rightarrow 6\,^2P_{3/2,1/2}$ is shown in Fig. 3. A frequency-doubled Quanta-Ray Pro Series pulsed Nd:YAG laser (10 Hz, 0–1 J/pulse, 532 nm) is used to pump a Sirah model PRSC-D-1800 dye laser with LDS-765 dye tuned to populate the Cs $7\,^2D_{3/2}$ or $7\,^2D_{5/2}$ levels. The dye laser provides 6–10 ns pulses in a 1 mm radius spot as the energy is tuned from 0 to 30 mJ/pulse by varying the Nd:YAG flash-lamp energy. The Cs DPAL cell path is a 12 cm long and 2.54 cm diameter heat pipe [28]. The rare-gas species, He or Ar, was monitored by two MKS Instruments 690A Baratron capacitance manometers with ranges of 1000 and 10 Torr. An aluminum heater block encloses the cell with a Watlow temperature controller connected to eight cartridge heaters and a thermocouple on a negative-feedback loop to control the cell temperature. Experiments were conducted at Cs DPAL cell temperatures of 25 °C, 35 °C, 40 °C, and 50 °C to vary Cs alkali-metal concentration and minimize the effect of radiation trapping on the spin-orbit mixing rate.

The target states, Cs $7\,^2D_{3/2}$ and Cs $7\,^2D_{5/2}$, are produced by two-photon absorption of the ground state, Cs $6\,^2S_{1/2}$, at wavelengths near 767.8 and 767.2 nm, respectively. The population of each excited state is measured by detecting the fluorescence measured by the C31034A photomultiplier tube using narrow bandpass filters and a BK 7 biconvex lens with a diameter of 50.8 mm and focal length of 88.3 mm to observe two different transition states, Cs ($7\,^2D_{3/2} \rightarrow 6\,^2P_{1/2}$) at 672.3 nm and Cs ($7\,^2D_{5/2} \rightarrow 6\,^2P_{3/2}$) at 697.3 nm. A Thorlabs FES0750 shortpass filter with a cutoff wavelength of 750 nm was used to minimize scattered pump light yet allow over 88% transmission for both 672.3 and 697.3 nm fluorescence emissions. For the 672.3 nm emission, a second Andover Corp 670.8 nm filter with center wavelength and 10 nm bandwidth filter was used in conjunction with the shortpass filter. The 670.8 nm filter has a 66% transmission at 672.3 nm. For 697.3 nm, an Andover Corp 697.3 nm center wavelength filter with a 1 nm bandwidth was used with the shortpass filter. The tighter bandwidth requirement for 697.3 nm is needed to reduce fluorescence emissions from the Cs ($7\,^2D_{3/2} \rightarrow 6\,^2P_{3/2}$) transition at 698.3 nm. The peak transmission for this filter at 697.3 nm is 47%. For each pressure the scattered pump laser intensity was measured and subtracted from the observed decay profiles by tuning off resonance, thereby minimizing the scattered light contribution to the $7\,^2D$ state on-resonance fluorescence signal.

The observed intensities for the 672.3 and 697.3 nm emissions, I_1 and I_2, are proportional to the concentration of the corresponding emitting states

$$I_1 \propto [Cs_{7\,^2D_{3/2}\rightarrow 6\,^2P_{1/2}}]d_1 \propto n_1 d_1, \tag{16}$$

$$I_2 \propto [Cs_{7\,^2D_{5/2}\rightarrow 6\,^2P_{3/2}}]d_2 \propto n_2 d_2, \tag{17}$$

where d_1, d_2 depend on detection system efficiencies, transition probabilities, and radiometric factors. The fluorescence of the Cs signal consists of 1000 laser shots summed averaged using a 3 GHz LeCroy WavePro 7300 oscilloscope.

IV. RESULTS

To validate that Cs alkali-metal atoms were pumped by two-photon absorption, excitation spectra using the time-integrated 697 and 672 nm fluorescence intensities as the signals were performed. The spectra for the cesium cell at 35 °C for these two emissions are shown in Fig. 4. When monitoring the emission from $7\,^2D_{5/2}$ at 697 nm, a signal is observed only when directly pumping the same state, confirming that the 1 nm bandpass filter is sufficient to isolate emission from $7\,^2D_{5/2}$. When pumping $7\,^2D_{3/2}$ a weak signal can be observed from the $7\,^2D_{5/2}$ state, suggesting minor Cs-induced mixing. A very slow scan across a single feature reveals the ground $6\,^2S_{1/2}$ fine-structure splitting with incomplete resolution, consistent with a laser linewidth of about 0.06 cm^{-1}.

All the intensity decay measurements for the He and Ar collision partners were performed at temperatures $\leq$ 50 °C. As shown in Fig. 5, temperatures above 75 °C resulted in longer decay rates caused by radiation being absorbed and re-emitted before escaping the heat pipe.

The time-resolved fluorescence from the collisionally populated $7\,^2D_{3/2}$ state after two-photon excitation of the $7\,^2D_{5/2}$ state for various helium pressures is provided in Fig. 6. The rate for fine-structure mixing is very rapid. Even at 0.1 Torr of helium, a significant population is observed with a peak occurring 60 ns after excitation. At 7 Torr the rise time is shorter than the pump pulse duration and only the longer quenching decay can be observed. At the higher pressures the

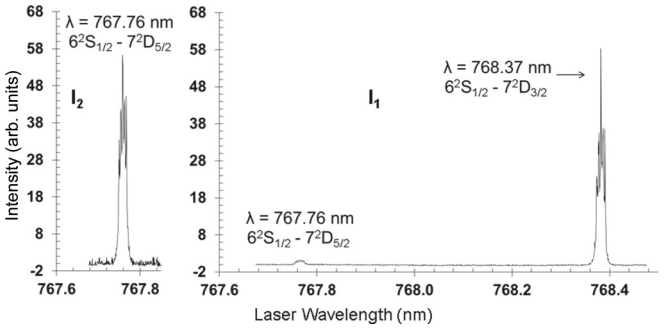

FIG. 4. Laser excitation spectra using the time-integrated fluorescence intensity at 697 and 672 nm.

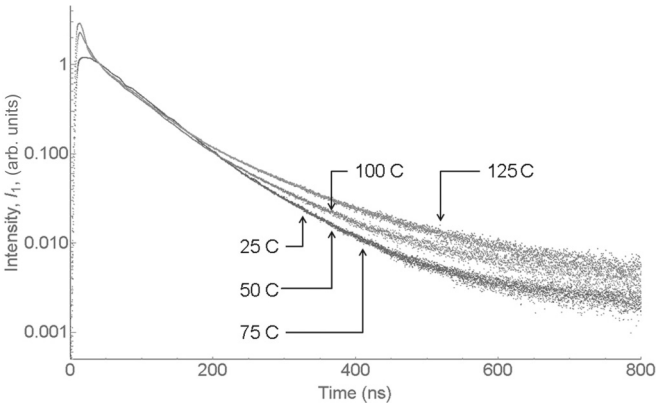

FIG. 5. Emission intensity I_1 from $7\,^2D_{3/2}$ when pumping the same $7\,^2D_{3/2}$ state at several Cs cell temperatures and no added buffer gas. The intensities grow dramatically with temperature, but have be normalized to the same value just after the laser pulse to illustrate the radiation trapping at $T > 75\,^\circ$C.

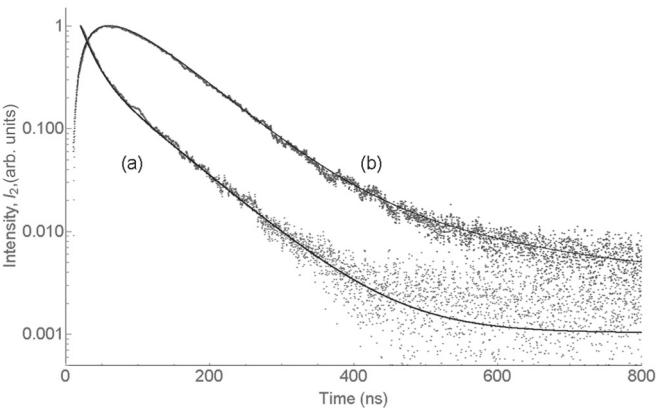

FIG. 7. Emission on $7\,^2D_{5/2} \rightarrow 6\,^2P_{3/2}$ at 697 nm after excitation on $7\,^2D_{3/2}$ for Ar pressures of (a) 50 and (b) 0.7 Torr. A fit to Eq. (7) is also provided.

peak signal decreases due to quenching during the excitation pulse.

For each pressure, the decay curves, such as those in Fig. 7, were fit to the double-exponential function of Eq. (7) generating the two eigenvalues. The pressure dependence of the fit eigenvalues are displayed as Stern-Volmer plots for He in Fig. 8 and similar curves were analyzed for Ar.

For He, the experimentally calculated spin-orbit rate is derived from the slope of eigenvalue λ_+ as shown in Fig. 8. The slope is $3.1 \pm 0.1 \times 10^{-9}$ cm^3/s yielding a fine structure relaxation rate of $k_{21} = 1.26 \pm 0.05 \times 10^{-9}$ cm^3/s. From the slope of λ_- we obtain the quenching rate $k_Q = 6.84 \pm 0.09 \times 10^{-11}$ cm^3/s. For an average temperature of 40 °C, the respective spin-orbit and quenching cross sections are $\sigma_{21} = 9.6 \pm 0.4 \times 10^{-15}$ cm^2 and $\sigma_Q = 5.25 \pm 0.07 \times 10^{-16}$ cm^2, respectively. The uncertainty in the cross sections represent the 95% confidence bounds in the unweighted linear fits. Similarly, for Ar, the calculated spin-orbit rate is $k_{21} = 1.52 \pm 0.05 \times 10^{-10}$ cm^3/s and the quenching rate is $k_Q = 2.65 \pm 0.04 \times 10^{-11}$ cm^3/s. For an average temperature of 40 °C, the respective spin-orbit and quenching cross sections are $\sigma_{21} = 3.3 \pm 0.1 \times 10^{-15}$ cm^2 and $\sigma_Q = 5.67 \pm 0.09 \times 10^{-16}$ cm^2, respectively. The intercept for the helium Stern-Volmer plot provides a collisionless lifetime of 148 ± 42 ns, with the lower bound near the radiative lifetime measurement of 98 ns [29].

V. DISCUSSION

Figure 9 shows experimental Cs-He and Cs-Ar cross sections, converted into probabilities and plotted against their respective adiabaticities. The $7\,^2D$ cross-section measurements are combined with the Cs-He and Cs-Ar collision database ($8\,^2P$, $7\,^2P$, and $6\,^2P$) values discussed in the recent adiabaticity study [22]. The fine-structure splitting for Cs $7\,^2D$ is 21 cm^{-1} compared to the 83 cm^{-1} for Cs $8\,^2P$, 181 cm^{-1} for Cs $7\,^2P$, and 554 cm^{-1} for Cs $6\,^2P$. The current results represent more impulsive, less adiabatic collision conditions, resulting in higher transfer probabilities. For the same adiabaticity, the high polarizability of the rare-gas collision partners enhances the transfer probability [22]. The atom polarizability increases the interaction length which is directly proportional to adiabaticity. It is unlikely that the added channel of rovibrational excitation in a molecular collision partner will significantly increase the

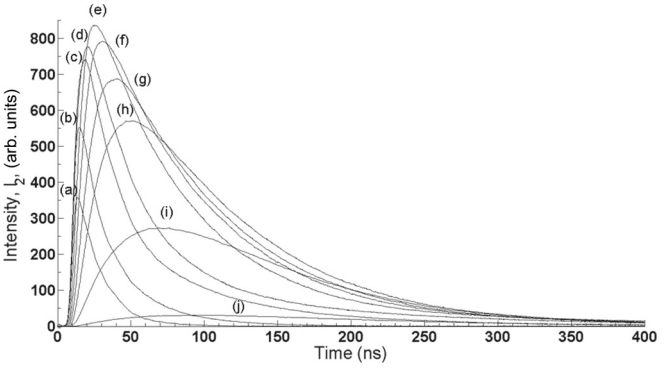

FIG. 6. Fluorescence decay curves of the Cs $7\,^2D_{3/2} \rightarrow 6\,^2P_{1/2}$ emission after excitation of $7\,^2D_{5/2}$ at 50 °C for helium buffer gas pressures in Torr (a) 100, (b) 50, (c) 15, (d) 7, (e) 2, (f) 1, (g) 0.5, (h) 0.25, (i) 0.1, and (j) 0.

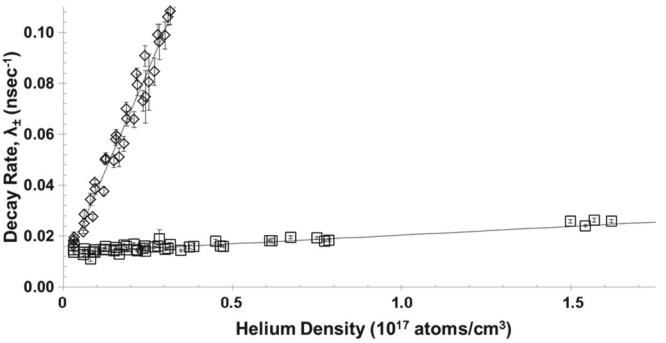

FIG. 8. Stern-Volmer plot of experimentally derived rates based on Eq. (7) for helium at temperatures $\leqslant 50\,^\circ$C. The solid line is a least-squares linear fit to the experimentally derived rates.

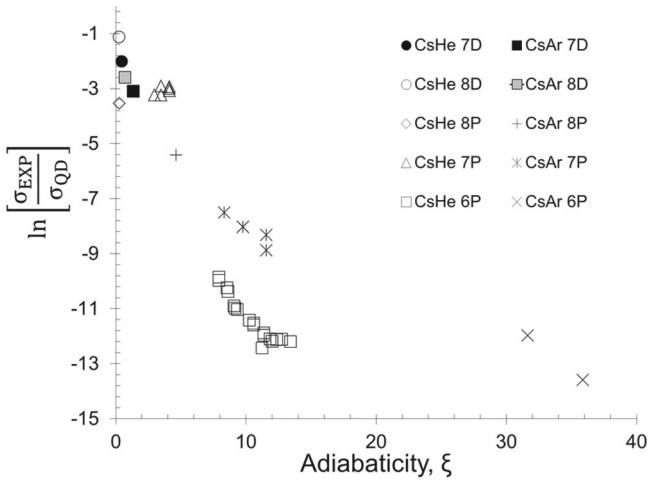

FIG. 9. Log probabilities plotted against the calculated adiabaticities where open and closed symbols represent Cs-He and Cs-Ar collisions, respectively, for different energy states. The open and closed circles represent the experimental 7 ^2D measurements from this study.

transfer rate, as has been characterized for Rb $5P$ [30]. The rare-gas collision probability is already very high.

VI. CONCLUSIONS

Collision-induced mixing between the Cs 7 $^2D_{5/2,3/2}$ states is exceptionally fast, driven by the large radius of the valence electron and small energy splitting. The helium rate exceeds that for argon by a factor of 7.4 due to both the higher relative speed and the more impulsive nature of the collision. The quenching rates are moderately fast, but 46 and 16 times slower than the mixing rates for helium and argon, respectively. The rates suggest efficient lasing may be achieved on several competing transitions.

ACKNOWLEDGMENTS

The authors thank Aaron Archibald and Chris Rice for their preliminary laboratory work on this project.

[1] A. L. Schawlow and C. H. Townes, Phys. Rev. **112**, 1940 (1958).
[2] W. F. Krupke, Diode-pumped alkali laser, U.S. Patent 6643311 (2003).
[3] W. F. Krupke, R. J. Beach, V. K. Kanz, and S. A. Payne, Opt. Lett. **28**, 2336 (2003).
[4] W. F. Krupke, Prog. Quantum Electron. **36**, 4 (2012).
[5] G. D. Hager and G. P. Perram, Appl. Phys. B **101**, 45 (2010).
[6] G. Hager and G. Perram, Appl. Phys. B **112**, 507 (2013).
[7] B. V. Zhdanov and R. J. Knize, Opt. Eng. **52**, 021010 (2013).
[8] F. Gao, F. Chen, J. J. Xie, D. J. Li, L. M. Zhang, G. L. Yang, J. Guo, and L. H. Guo, Optik **124**, 4353 (2013).
[9] M. Auzinsh, R. Ferber, F. Gahbauer, A. Jarmola, L. Kalvans, and A. Atvars, Opt. Commun. **284**, 2863 (2011).
[10] K. C. Brown and G. P. Perram, Opt. Commun. **300**, 51 (2013).
[11] K. C. Brown and G. P. Perram, Proc. SPIE **7915**, 791507 (2011).
[12] K. C. Brown and G. P. Perram, Phys. Rev. A **85**, 022713 (2012).
[13] P. Chaves de Souza Segundo, I. Hamdi, M. Fichet, D. Bloch, and M. Ducloy, Laser Phys. **17**, 983 (2007).
[14] J. Huennekens, Z. Wu, and T. G. Walker, Phys. Rev. A **31**, 196 (1985).
[15] G. P. Perram, Proc. SPIE **8381**, 838109 (2012).
[16] G. A. Pitz, C. V. Sulham, E. Acosta, and G. P. Perram, *AIAA 41st Plasmadynamics and Lasers Conference, Chicago, IL, 28 June - 1 July 2010* (American Institute of Aeronautics and Astronautics, Reston, VA, 2010), Paper 4876.
[17] A. Sharma, Appl. Phys. Lett. **39**, 209 (1981).
[18] C. V. Sulham, G. A. Pitz, and G. P. Perram, Appl. Phys. B **101**, 57 (2010).
[19] G. P. Perram, S. J. Cusumano, R. L. Hengehold, and S. T. Fiorino, *An Introduction to Laser Weapon Systems* (Directed Energy Professional Society, Albuquerque, NM, 2009).
[20] P. V. Kiran Kumar, M. Sankari, and M. V. Suryanarayana, Phys. Rev. A **87**, 012503 (2013).
[21] Y. C. Lee, Y. H. Chang, Y. Y. Chang, Y. Y. Chen, C. C. Tsai, and H. C. Chui, Appl. Phys. B **105**, 391 (2011).
[22] B. Eshel, D. E. Weeks, and G. P. Perram, Proc. SPIE **8962**, 896207 (2014).
[23] A. Gallagher, Phys. Rev. **172**, 88 (1968).
[24] J. F. Sell, M. A. Gearba, B. M. Patterson, D. Byrne, G. Jemo, T. C. Lilly, R. Meeter, and R. J. Knize, J. Phys. B **45**, 055202 (2012).
[25] A. Sasso, W. Demtroder, T. Colbert, C. Wang, E. Ehrlacher, and J. Huennekens, Phys. Rev. A **45**, 1670 (1992).
[26] C. E. Theodosiou, Phys. Rev. A **30**, 2881 (1984).
[27] J. Elward-Berry and M. J. Berry, J. Chem. Phys. **72**, 4500 (1980).
[28] W. Klennert, A. J. Sandoval, and D. A. Hostutler, J. Directed Energy **4**, 245 (2012).
[29] J. Marek, Phys. Lett. A **60**, 190 (1977).
[30] M. D. Rotondaro and G. P. Perram, Phys. Rev. A **57**, 4045 (1998).